

# Monte Carlo Simulation of Operator Dynamics and Entanglement in Dual-Unitary Circuits

Menghan Song,<sup>1</sup> Zhaoyi Zeng,<sup>2</sup> Ting-Tung Wang,<sup>1</sup> Yi-Zhuang You,<sup>3,\*</sup> Zi Yang Meng,<sup>1,†</sup> and Pengfei Zhang<sup>2,4,5,6,‡</sup>

<sup>1</sup>*Department of Physics and HK Institute of Quantum Science & Technology,  
The University of Hong Kong, Pokfulam Road, Hong Kong SAR, China*

<sup>2</sup>*Department of Physics, Fudan University, Shanghai, 200438, China*

<sup>3</sup>*Department of Physics, University of California, San Diego, California 92093, USA*

<sup>4</sup>*State Key Laboratory of Surface Physics, Fudan University, Shanghai, 200438, China*

<sup>5</sup>*Shanghai Qi Zhi Institute, AI Tower, Xuhui District, Shanghai 200232, China*

<sup>6</sup>*Hefei National Laboratory, Hefei 230088, China*

(Dated: October 4, 2024)

We investigate operator dynamics and entanglement growth in dual-unitary circuits, a class of locally scrambled quantum systems that enables efficient simulation beyond the exponential complexity of the Hilbert space. By mapping the operator evolution to a classical Markov process, we perform Monte Carlo simulations to access the time evolution of local operator density and entanglement with polynomial computational cost. Our results reveal that the operator density converges exponentially to a steady-state value, with analytical bounds that match our simulations. Additionally, we observe a volume-law scaling of operator entanglement across different subregions, and identify a critical transition from maximal to sub-maximal entanglement growth, governed by the circuit's gate parameter. This transition, confirmed by both mean-field theory and Monte Carlo simulations, provides new insights into operator entanglement dynamics in quantum many-body systems. Our work offers a scalable computational framework for studying long-time operator evolution and entanglement, paving the way for deeper exploration of quantum information dynamics.

## I. INTRODUCTION

In quantum many-body physics, the study of operator dynamics is an active area of research. The dynamics of quantum operators under Heisenberg picture time evolution can provide insights into the complex behavior of quantum many-body systems, including operator spreading [1–10], scrambling and thermalization [11–21]. Simulating operator dynamics in quantum many-body systems is generally challenging due to the curse of dimensionality—the exponential growth of the Hilbert space with system size. While efficient computational methods exist in specific cases, such as Clifford circuits [22], time-evolving block decimation (TEBD) [23–25], or systems with partial integrability [26, 27], a general solution remains elusive.

When focusing solely on the statistical properties of *operator dynamics*, i.e. how the size and support of an operator evolves on average without concern for the specific operator content, more efficient approaches become available [3, 4, 7, 28, 29]. For *locally scrambled* quantum dynamics [15, 16], where the unitary evolution operators are weakly symmetric [30, 31] under local basis transformations, the operator dynamics can be mapped to an effective classical diffusion model in the space of operator supports [3, 29, 32]. This mapping simplifies the quantum evolution into a tractable classical Markov process,

allowing for efficient simulation via Monte Carlo (MC) sampling.

Furthermore, to characterize the internal complexity and correlations within an operator, the concept of *operator entanglement* has been introduced [33–36]. Operator entanglement quantifies the entanglement of the corresponding Choi state representation [37, 38] of the operator in the operator Hilbert space (a.k.a. doubled Hilbert space). In the context of operator dynamics, it characterizes how the information encoded by the initial operator scrambles with time and becomes correlated across different parts of the system over time. Nicely, we found that the second Rényi operator entanglement can also be studied under reasonable assumptions using above-mentioned Monte Carlo approach for operator dynamics on multiple replicas, enabling efficient computation of these quantities in complex systems.

In this work, we investigate the operator dynamics and operator entanglement in *dual-unitary circuits*—a class of quantum circuits consisting of dual-unitary gates, which are unitary in both space and time directions [35, 36, 39]. Dual-unitary circuits, like Haar random unitary circuits, are examples of locally scrambled quantum dynamics that enable operator dynamics to be studied efficiently by mapping to classical diffusion processes. However, compared to Haar random unitary gates, dual-unitary gates form a family of random unitary ensembles with tunable scrambling power controlled by a single parameter. This tunability allows us to systematically explore different scrambling behaviors within the same theoretical framework.

We demonstrate, via Monte Carlo simulations of the local operator density and entanglement in a dual-unitary

---

\* yzyou@physics.ucsd.edu

† zymeng@hku.hk

‡ pengfeizhang.physics@gmail.com

circuit, that the operator density near the light cone converges exponentially to  $\frac{3}{4}$ , with a rate determined by the gate parameter  $\alpha$ . In the long-time limit, we derive analytical bounds for the density profile, validated by Monte Carlo simulations. For operator entanglement, we observe volume-law scaling across different subregions, with the volume-law coefficient's dependence on  $\alpha$  varying. A key finding is the transition from maximal to sub-maximal entanglement growth for left movers at the left light cone, consistent with prior theoretical work [35, 36, 39, 40]. Our study provides a direct mapping of the volume-law coefficient to  $\alpha$ , confirmed by mean-field (MF) theory and Monte Carlo simulations, offering new insights into operator dynamics and entanglement transitions in dual-unitary circuits.

## II. LOCALLY-SCRAMBLED DUAL-UNITARY DYNAMICS

To introduce the concept of a dual-unitary gate, we consider an arbitrary two-qubit gate  $U$ . In the computational basis, its space-time dual  $\tilde{U}$  can be defined as

$$\tilde{U} := \sum_{ijkl} |kl\rangle \langle ik| U |jl\rangle \langle ij|, \quad (1)$$

The unitary  $U$  is called dual-unitary when its space-time dual  $\tilde{U}$  is also a unitary operator, satisfying  $U^\dagger U = \tilde{U}^\dagger \tilde{U} = I$  [39]. For qubit systems, dual unitary gates are parameterized by four single-qubit unitaries  $u_\pm, v_\pm$ , and a single parameter  $J$ :

$$U(J) = (u_+ \otimes u_-) e^{-i\frac{\pi}{4}(X_1 X_2 + Y_1 Y_2) - iJ Z_1 Z_2} (v_+ \otimes v_-). \quad (2)$$

Here,  $\{X_j, Y_j, Z_j\}$  are the Pauli operators on the  $j$ -th qubit. Single-qubit gates provide local basis rotations but do not entangle different sites. The non-trivial entanglement arises from the XXZ coupling, where  $J \in [0, \pi/4]$  characterizes the scrambling ability of the dual-unitary gate. For  $J = \pi/4$ ,  $U$  reduces to a SWAP operation, simply interchanging operators between two sites. Conversely, for  $J = 0$ , it maximally spreading single-site operators to operators supported on both sites.

In this work, we study the operator dynamics of random dual-unitary circuits for qubit systems arranged in a brick-wall architecture, as shown in Fig. 1 (a). The evolution operator is given by  $U_{\text{tot}}(t_f) = \prod_{t=1}^{t_f} U_t$ , where

$$U_t = \begin{cases} \bigotimes_k U_{2k-1, 2k} & \text{if } t \in \text{odd,} \\ \bigotimes_k U_{2k, 2k+1} & \text{if } t \in \text{even.} \end{cases} \quad (3)$$

Here,  $U_{x,x'}$  represent two-qubit dual-unitary gates acting on nearest-neighbor qubits  $x$  and  $x'$ . We note that throughout this paper, we use  $U$  to denote the quantum evolution operator and  $T$  the transfer matrix after mapping the dual-unitary quantum circuit to the classical Markov process. We sample each two-qubit gate  $U$  independently in the locally-scrambled dual-unitary ensemble

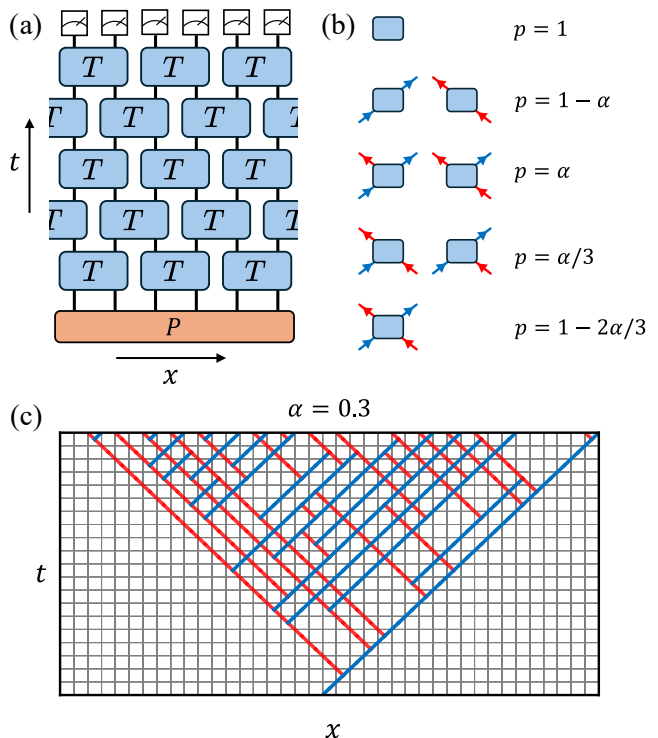


FIG. 1. **Schematic plot of a dual-unitary circuit which evaluates the Pauli weight  $w(P)$  on a Pauli string  $P$ .** (a) The brick-wall structure of local dual-unitary gates as transfer matrices  $T$ . The circuit takes a Pauli string  $P = \otimes_i P_i$  as an input, where local Pauli matrix  $P_i \in \{I, X, Y, Z\}$ . Operators  $\{X, Y, Z\}$  and  $I$  are capsuled as  $\frac{1}{3}|1\rangle$  (occupied) and  $|0\rangle$  (unoccupied) respectively. The final measurement layer projects the Pauli weight onto the basis  $\{|0\rangle, \frac{1}{3}|1\rangle\}$  at each site. (b) Each transfer matrix (rectangular 4-leg tensor) describes a segment in the Markov process that converts the state of two adjacent sites into another in the 2-site Hilbert space, i.e.,  $\{|00\rangle, |01\rangle, |10\rangle, |11\rangle\}$ . We denote an occupied site  $|1\rangle$  as a blue right-mover (red left-mover) if its space-time coordinate follows  $x+t = 0(1) \pmod{2}$ , and unoccupied state  $|0\rangle$  as lack of left or right movers. The eight vertices with non-zero probability are shown. (c) demonstrates one configuration generated by Monte Carlo simulation according to the Markov process in (b), with only one site being occupied in the middle at  $t=0$ . Both left and right movers evolve at the speed of light and create a light-cone trajectory.

from the distribution  $p(U|J)$  condition on the parameter  $J$ , and define the random unitary ensemble  $\mathcal{E}_J$ :

$$\mathcal{E}_J = \{U \sim p(U|J) = du_+ du_- dv_+ dv_-\}, \quad (4)$$

where  $du_\pm$  and  $dv_\pm$  represent the Haar measure of single-qubit rotations. This choice eliminates local basis dependence and is essential to mapping the full quantum dynamics to a classical Markov process [15], which then admits efficient Monte Carlo simulations, as we showed in this paper.

We are interested in the dynamical evolution of simple operators  $O$ . At time  $t$ , the Heisenberg evolution is given by  $O(t+1) = U_t^\dagger O(t) U_t$ . For later convenience, we rep-

represent the operator  $O$  as a state  $|O\rangle$  in a doubled Hilbert space, known as the Choi representation [37, 38]. On a complete set of orthonormal basis  $\{|i\rangle\}$  of the Hilbert space, under the operator-state mapping, any generic operator  $O = \sum_{ij} |i\rangle O_{ij} \langle j|$  gets mapped to a corresponding doubled state as  $|O\rangle = 2^{-L/2} \sum_{ij} O_{ij} |i\rangle \otimes |j\rangle$ . Here,  $L$  denotes the system size. In this language, the Heisenberg evolution reads  $|O(t+1)\rangle = (U_t^\dagger \otimes U_t^T)|O(t)\rangle$ . We choose a orthogonal basis in the operator space at site  $x$  as  $\{|I\rangle_x, |X\rangle_x, |Y\rangle_x, |Z\rangle_x\}$ , where each basis state corresponds to having the operator  $\{I, X, Y, Z\}$  acting on the qubit  $x$ , respectively. The operator wavefunction can be expanded as

$$|O(t)\rangle = \sum_P c_P(t) |P\rangle, \quad (5)$$

where  $|P\rangle = |P_{-L/2} P_{-L/2+1} \dots P_{L/2-1}\rangle$  with  $P_x \in \{I, X, Y, Z\}$ . We study the growth of a local operator that initially acts near the middle of the system (around  $x \approx 0$ ), focusing on the time regime before it reaches the system boundaries under the operator dynamics, so that boundary effects remain irrelevant.

### A. Operator Density

We investigate the operator dynamics by monitoring both the evolution of operator density [3] and the operator entanglement entropy [36]. The operator density  $\rho(x, t)$  is defined as the probability of finding a non-trivial operator on site  $x$ :

$$\rho(x, t) = \sum_{\{P|P_x \neq I\}} \overline{|c_P(t)|^2} \equiv \sum_{\{P|P_x \neq I\}} w_P(t). \quad (6)$$

Here, the overline denotes the ensemble average over the realizations of random single-qubit gates in the dual-unitary ensemble. There are great simplifications if we focus on locally-scrambled quantum circuits: the phase of  $c_P(t)$  exhibits random fluctuations due to the random single-qubit rotations, and the evolution of  $w_P(t)$  becomes Markovian [15]. The evolution generated by each two-qubit gate  $U_{xy}$  reads

$$w_P(t) \rightarrow w_P(t+1) = \sum_{P'} T^{(2)}(P_x P_y, P'_x P'_y) w_{P'}(t), \quad (7)$$

where the summation  $\sum'$  is restricted to the subspace where  $P'_z = P_z$  for any  $z \neq x, y$ . The  $16 \times 16$  transfer matrix  $T^{(2)}$  is computed in a two-qubit system by

$$\begin{aligned} T^{(2)}(P, P') &:= \overline{|\langle P|(U^\dagger \otimes U^T)|P'\rangle|^2} \\ &= \frac{1}{2^4} \int_{U \in \mathcal{E}_J} dU |\text{tr}(PU^\dagger P'U)|^2. \end{aligned} \quad (8)$$

The completeness of Pauli operators guarantees the conservation of the probability, as  $\sum_P T^{(2)}(P, P') = 1$ .

Furthermore, we observe that the absence of local basis dependence suggests that  $T^{(2)}(P, P')$  only depends on the support of  $P$  and  $P'$ . As a consequence,  $w_P(t)$  at  $t > 0$  also depends only on the support of  $P$  rather than on the specific content of the Pauli string  $P$ . To eliminate the redundancy in  $w_P$ , we introduce a bit string  $b = b_{-L/2} b_{-L/2+1} \dots b_{L/2-1}$  to denote the support of a Pauli string, where  $b_x \in \{0, 1\}$ . We use  $b_x = 0$  to indicate the case where the site  $x$  is not occupied by the operator and  $b_x = 1$  for the occupied case. Then, we can rewrite the Markov process in this occupation basis, where the transfer matrix can be reduced to a  $4 \times 4$  matrix  $T$ . Introduce  $w_b(t) = 3^{|b|} w_P(t)$ , where  $P$  is an arbitrary Pauli operator of support  $b$ , with  $|b|$  denoting the number of occupied sites in the bit string  $b$  (i.e. the operator size), and the factor  $3^{|b|}$  counts the total number of Pauli operators of the same support  $b$ . The operator density  $\rho(x, t)$  can be expressed as

$$\rho(x, t) = \sum_{\{b|b_x=1\}} w_b(t). \quad (9)$$

Defining  $T(b, b') = 3^{|b|} T^{(2)}(P, P')$ , the evolution generated by each two-qubit gate remains

$$w_b(t) \rightarrow w_b(t+1) = \sum_{b'} T(b_x b_y; b'_x b'_y) w_{b'}(t), \quad (10)$$

where the summation  $\sum'$  is again restricted to the subspace where  $b'_z = b_z$  for any  $z \neq x, y$ . The full Markovian dynamics is then represented by a brick-wall circuit of local transfer matrices  $T$ , as illustrated in Fig. 1 (a). For the locally-scrambled dual-unitary ensemble, the explicit expression of  $T(b, b')$  for each two-qubit gate has been computed [40], which reads

$$T(b, b') = \begin{pmatrix} 1 & 0 & 0 & 0 \\ 0 & 0 & 1 - \alpha & \alpha/3 \\ 0 & 1 - \alpha & 0 & \alpha/3 \\ 0 & \alpha & \alpha & 1 - 2\alpha/3 \end{pmatrix}_{bb'}, \quad (11)$$

with parametrization  $\alpha = \frac{2}{3} \cos^2(2J) \in [0, 2/3]$  that controls the information scrambling power of the dual-unitary gate ensemble:  $\alpha = 0$  corresponds to the SWAP gate with no scrambling, and  $\alpha = 1$  corresponds to the fastest scrambling dual unitary gates.

### B. Operator Entanglement

We also examine the growth of operator entanglement in the random dual-unitary circuit [35, 36]. After mapping the operator to a state, the operator entanglement  $O(t)$  for a subregion  $A$  of the original qubit system is defined as the conventional entanglement entropy of the corresponding Choi state  $|O(t)\rangle$  for the same subregion, as illustrated in Fig. 2.

More explicitly, we first construct the reduced density matrix in the operator space

$$\rho_A[O(t)] = \text{tr}_{\bar{A}} |O(t)\rangle \langle O(t)|. \quad (12)$$

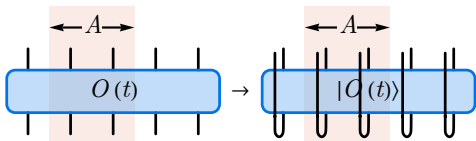


FIG. 2. Illustration of operator-state mapping and operator entanglement in region  $A$ .

Here,  $\bar{A}$  denotes the complement of the subregion  $A$ . We can compute either the von Neumann entropy  $S_A(t) = -\text{tr}_A(\rho_A \log \rho_A)$  or the  $n$ -th Rényi entropy  $S_A^{(n)}(t) = \frac{1}{1-n} \log \text{tr}(\rho_A^n)$ . In this work, we focus on small subsystem size  $|A| \ll |\bar{A}|$ , where theoretical analysis becomes more tractable after the following approximations regarding the disorder average:

$$\begin{aligned} \overline{S_A^{(n)}}(t) &= -\frac{1}{n-1} \overline{\log \text{tr}(\rho_A^n)} \approx -\frac{1}{n-1} \log \text{tr}(\overline{\rho_A^n}) \\ &\approx -\frac{1}{n-1} \log \text{tr}(\overline{\rho_A}^n). \end{aligned} \quad (13)$$

In the first step, we approximate the disorder average of the entropy by the disorder average of  $\text{tr}(\rho_A^n)$ . This approximation assumes that the corresponding variance is negligible within the ensemble of random circuits [41, 42]. However, the calculation still requires the disorder average over  $2n$ -replicas  $U^{\otimes 2n} \otimes (U^\dagger)^{\otimes 2n}$ , where the Schur-Weyl duality suggests that the effective degrees of freedom are elements of the  $S_{2n}$  group. To further simplify the calculation, we assume that  $S_A^{(n)}$  is dominated by the “replica diagonal” contribution for small subsystems  $|A|$ , allowing us to replace  $\overline{\rho_A^n}$  with  $\overline{\rho_A}^n$ , which constitutes our second step. It is known that these approximations become exact if we consider a system with qudits and take the limit of a large local Hilbert space dimension ( $d \rightarrow \infty$ ) [36].

Under this approximation, we can express the second Rényi entropy in terms of  $w_b(t)$ . As explained in Sec. II A, the disorder-averaged operator density matrix contains only the diagonal components:  $\overline{\rho} = \frac{|O(t)\rangle\langle O(t)|}{\langle O(t)|O(t)\rangle} = \sum_P w_P(t) |P\rangle\langle P|$ . Tracing out the subregion  $\bar{A}$ , we obtain the reduced density matrix

$$\overline{\rho_A} = \sum_{P_A, P_{\bar{A}}} w_{P_A P_{\bar{A}}}(t) |P_A\rangle\langle P_A| \equiv \sum_{P_A} w_{P_A}(t) |P_A\rangle\langle P_A|, \quad (14)$$

where we have decomposed  $P = P_A \otimes P_{\bar{A}}$  and introduced the marginal distribution  $w_{P_A}(t) = \sum_{P_{\bar{A}}} w_{P_A P_{\bar{A}}}(t)$ . The purity of the system is then computed by

$$e^{-(n-1)\overline{S_A^{(n)}}(t)} \approx \sum_{P_A} w_{P_A}^n(t) = \sum_{b_A} \frac{1}{3^{|b_A|(n-1)}} w_{b_A}^n(t), \quad (15)$$

where  $b_A$  denotes a bit string defined in region  $A$ .

### C. Monte Carlo Simulation

Since  $w_b(t)$  contains an exponentially large number of components, indexed by the bit string  $b = \{b_x\}$  (with  $b_x \in \{0, 1\}$ ) that labels the operator support. Direct analytical or numerical study of the evolution of  $w_b(t)$  following Eq. (10) is impractical. To this end, we would like to use the Monte Carlo method to carry out important sampling and reduce the exponential computation to polynomial complexity. We may interpret the operator support  $b$  as an occupation configuration of some fictitious “particles”, and visualize the Markovian dynamics of operator evolution as the evolution of classical particles, where each lattice site  $x$  is either empty ( $b_x = 0$ ) or occupied by a particle ( $b_x = 1$ ). The system is initialized according to the support of the initial operator  $O$ . The application of a transfer matrix in Eq. (11) on sites  $x$  and  $x+1$  is then implemented by the following local update rule, parametrized by the scrambling parameter  $\alpha$  of the dual unitary gate:

1. If both sites are unoccupied, no update is needed.
2. If only site  $x$  is occupied, we move the particle from site  $x$  to site  $x+1$ . With a probability of  $1-\alpha$ , site  $x$  is left empty. Otherwise, a new particle is added at site  $x$ .
3. If only site  $x+1$  is occupied, we move the particle from site  $x+1$  to site  $x$ . With a probability of  $1-\alpha$ , site  $x+1$  is left empty. Otherwise, a new particle is added at site  $x+1$ .
4. If both sites are occupied, the configuration is kept unchanged with a probability  $1-2\alpha/3$ . Otherwise, one of the two particles is randomly removed, and the probability to remove either particle is  $\alpha/3$ .

These update rules are graphically shown in Fig. 1 (b) and they reveal a central feature of dual-unitary circuits with a brick-wall architecture. In the absence of scattering with other particles, a particle continues to move in a single spatial direction. Therefore, it is natural to distinguish lattice sites corresponding to right movers and left movers based on the parity of  $x+t$ . As an illustration, we depict right movers in blue and left movers in red in Fig. 1 (c) for a typical evolution history.

Starting from any initial configuration of the operator support (equivalently viewed as “particle” occupation configuration) at time  $t=0$ , we can stochastically generate the configuration  $b$  at later time  $t$  following the update rules described above. These update rules ensure that the underlying probability distribution of  $b$  at time  $t$  will precisely match  $w_b(t)$ , as if we can effectively sample  $b$  from the distribution  $w_b(t)$ .

After collecting many independent samples, we can estimate the operator density  $\rho(x,t)$  by counting the average particle number at the corresponding space-time position. On the other hand, the operator entanglement entropy  $\overline{S_A^{(n)}}(t)$  is a non-linear function of the probability



distribution  $w_b(t)$ . In the Monte Carlo simulation, we focus on the second Rényi entropy with Rényi index  $n = 2$ . This first requires generating two independent configurations of classical particles at time  $t$ , labeled by their occupation bit strings  $b^{(1)}$  and  $b^{(2)}$ . Then, we compute

$$I(b^{(1)}, b^{(2)}) = \prod_{x \in A} 3^{-b_x^{(1)}} \delta_{b_x^{(1)} b_x^{(2)}} \quad (16)$$

as an estimator of Eq. (15). Here,  $\delta_{b_x^{(1)} b_x^{(2)}}$  is the Kronecker delta symbol that enforces  $b^{(1)}$  and  $b^{(2)}$  have identical configurations inside the entanglement region  $A$  of interest, otherwise the quantity  $I(b^{(1)}, b^{(2)})$  will be zero. Averaging  $I(b^{(1)}, b^{(2)})$  over many pairs of samples gives  $\langle e^{-\overline{S_A^{(2)}}} \rangle$ , and then  $\overline{S_A^{(2)}} = -\ln \langle I(b^{(1)}, b^{(2)}) \rangle$ .

As one can see from Eq. (16), a non-zero  $I$  is sampled only if  $b_x^{(1)} = b_x^{(2)}, \forall x \in A$ , which is an exponentially rare event to happen. This makes the sampling exponentially inefficient for estimating the operator entanglement. In practice, we mitigate this issue by computing the probability distribution at time  $t$  condition on the configuration generated at time  $t - 1$ , where  $t$  denotes the time slice where operator properties are measured. Recall that each local transfer matrix  $T$  acts on one pair of left and right movers, and is unrelated to the others pair of movers in the same time slice due to the brick-wall architecture. Therefore, for every two sites (a pair of movers), we can explicitly compute the probability of all four possible states in the 2-site state space occurring at  $t$ , conditioned on the current state at  $t - 1$ . Let's denote the particle configuration at time  $t$  by the bit string  $b = \{b_x\}$ , and that at time  $t - 1$  by the bit string  $b' = \{b'_x\}$ . Then we can compute the quantity  $I$  as a function of  $b^{(1)}$  and  $b^{(2)}$ , which are independently sampled in two replica up to the  $t - 1$  time step,

$$I(b^{(1)}, b^{(2)}) = \prod_{2k \in A} \sum_{b_{2k-1}, b_{2k}} 3^{-(b_{2k-1} + b_{2k})} \tilde{w}_{b|b^{(1)}} \tilde{w}_{b|b^{(2)}} \quad (17)$$

which amounts to directly summing over all the final-time configurations  $b$  based on the conditional probability  $\tilde{w}_{b|b^{(1)}} \tilde{w}_{b|b^{(2)}}$ . Here  $\tilde{w}_{b|b'}$  corresponds to the conditional probability to generate  $b$  given  $b'$  in a single replica, which is given by (the tensor product) of the transfer matrix  $T(b, b')$ , defined in Eq. (11),

$$\tilde{w}_{b|b'} = \prod_k T(b_{2k-1} b_{2k}; b'_{2k-1} b'_{2k-1}), \quad (18)$$

assuming the last time step is an odd step without loss of generality. In this way, averaging  $I(b^{(1)}, b^{(2)})$  also gives unbiased estimation of the operator entanglement  $\overline{S_A^{(2)}} = -\ln \langle I(b^{(1)}, b^{(2)}) \rangle$ . Since the summation of configurations  $b$  can be factorized to that on each pair of sites at  $(2k - 1, 2k)$ , which can be computed efficiently, we can now obtain a finite real number  $I(b^{(1)}, b^{(2)})$  from each Monte Carlo sampling instead of waiting an exponentially long time for  $\delta_{b_x^{(1)} b_x^{(2)}} = 1$  to occur. Similar approach in spirit, to overcome the exponential observable

with log-normal distribution to a typical observable with normal distribution [43–45], has been employed in the recent computation of entanglement entropy and other exponential observables in the quantum many-body systems within quantum Monte Carlo and Tensor Network setup [44, 46–53].

### III. RESULTS

In the following, we will investigate the operator dynamics and operator entanglement growth in dual-unitary circuits using the Monte Carlo sampling approach described above, and compare the results with mean-field theoretical understandings.

For the operator dynamics, we focusing on two initial operators:  $O = Z_0 Z_1$  and  $O = Z_1$ . For  $O = Z_0 Z_1$ , we find that the operator density evolution closely follows the mean-field approximation, with our analytical solutions in both the long-time limit and near the light-cone matching well with Monte Carlo simulations. Conversely, for  $O = Z_1$ , the operator density near the left light-cone deviates significantly from mean-field predictions due to strong correlations arising from the stochastic emission time of the first left-moving operator. By incorporating a conditional probability framework, we derive analytical expressions that accurately capture these correlations, achieving excellent agreement with numerical results.

Additionally, we explore operator entanglement growth in three different subregions near the light-cone and identify entanglement transitions as the parameter  $\alpha$  varies. Our analytical predictions of critical values for these transitions are validated by Monte Carlo simulations, which has not been observed in previous works [35, 36, 39, 40]. Our discovery therefore highlights the sensitivity of entanglement growth to initial conditions and system parameters.

Overall, our findings demonstrate the intricate interplay between operator dynamics, correlations, and entanglement scaling in dual-unitary circuits, enhancing the understanding of information spreading, thermalization, and quantum information scrambling in quantum many-body systems.

#### A. Operator Density Evolution

We begin with the analysis of operator density evolution. For illustration, we focus on two different initial operators:  $O = Z_0 Z_1$  (two-site operator) or  $O = Z_1$  (single-site operator), which turns out to show different features. According to our convention in Eq. (3),  $Z_0$  represents a left mover, while  $Z_1$  corresponds to a right mover. We present typical results of the operator density evolution in Fig. 3 (a) and (b) using solid lines for  $\alpha = 0.2$  and  $t = 16, 32$ . The data presented is averaged over  $10^7$  Monte Carlo steps such that error bars are negligible from bare-eye observation.

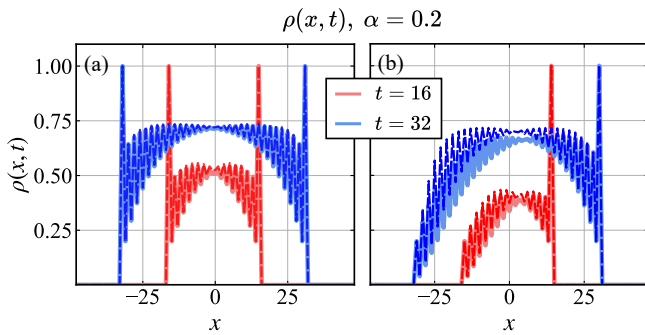


FIG. 3. **Comparing density profile obtained from the recurrence relation in Eq. (20) with Monte Carlo data at  $\alpha = 0.2$ .** Initially, panel (a) has two sites occupied in the middle and panel (b) has a single site occupied in the middle. In both panels, solid lines represent the Monte Carlo data with  $\sim 10^7$  samplings such that the error bar is negligible in the figure. The dashed lines are generated from the recurrence relation Eq. (20). The MF prediction matches well with the MC data with the two-site initial condition at any time  $t$ , while it deviates from the MC result at large  $t$  with a single-site initial condition.

### 1. Balanced operator growth from two-site operator

Let us first focus on the scenario with  $O = Z_0 Z_1$ . On both the left ( $x+t=0$ ) and right ( $x-t=1$ ) light-cones, the operator density is 1, consistent with the ballistic transport of the initial operator. Within this light-cone, the operator density continues to increase due to the creation of new particles at finite splitting probability  $\alpha$ . In the long-time limit, the operator density on each site  $x$  approaches  $3/4$ , indicating that each single-qubit Pauli operator  $\{I, X, Y, Z\}$  appears with equal probability, as expected for generic chaotic quantum systems [54]. To gain a more quantitative understanding, we adopt the zeroth-order mean-field approximation [40], which approximates the joint distribution  $w_b$  of the operator support  $b$  as product of independent Bernoulli distribution of  $b_x$  on each site  $x$ , parametrized by the operator density  $\rho(x, t)$  as

$$w_b(t) \approx \prod_x [b_x \rho(x, t) + (1 - b_x)(1 - \rho(x, t))]. \quad (19)$$

This mean-field approximation neglects any correlation between different sites. The evolution of  $\rho(x, t)$  is then derived by applying a layer of transfer matrix  $T$  and computing the post-evolution density  $\rho(x, t+1)$  [40]. For a transfer matrix  $T$  applied to sites  $x$  and  $x+1$ , the evolution reads

$$\begin{aligned} \rho(x, t+1) &= \rho(x+1, t) + \alpha \rho(x, t) \left(1 - \frac{4}{3} \rho(x+1, t)\right), \\ \rho(x+1, t+1) &= \rho(x, t) + \alpha \rho(x+1, t) \left(1 - \frac{4}{3} \rho(x, t)\right). \end{aligned} \quad (20)$$

The evolution generated by these equations is plotted in Fig. 3 (a) using dashed lines. The results match

the Monte Carlo simulation with high accuracy for  $O = Z_0 Z_1$ . Additionally, we provide analytical solutions in two limits:

1. In the long-time limit  $t \gg 1$  for a fixed lattice site  $x$ , we can neglect the spatial dependence of the operator density and expand  $\rho(t) = 3/4 - \delta\rho(t)$ . The evolution then becomes

$$\delta\rho(t+1) = (1 - \alpha)\delta\rho(t) + O(\delta\rho^2). \quad (21)$$

This equation can be solved exactly, which gives

$$\rho(t) \approx \frac{3}{4} - Ae^{-\lambda t}, \quad \text{with } \lambda = -\ln(1 - \alpha). \quad (22)$$

2. Now, we consider the near-light-cone steady state for the operator density. Specifically, we examine the case where  $d = x+t \sim O(1)$  or  $d = t-x+1 \sim O(1)$  with  $t \gg 1$ . Numerical results suggest the existence of a steady-state distribution  $\rho_d^{\text{LC}}$ , where LC stands for ‘‘light-cone’’, which satisfies  $\rho_0^{\text{LC}} = 0$ ,  $\rho_1^{\text{LC}} = 1$  and

$$\begin{aligned} \rho_{2k}^{\text{LC}} &= \rho_{2k}^{\text{LC}} + \alpha \rho_{2k-1}^{\text{LC}} \left(1 - \frac{4}{3} \rho_{2k}^{\text{LC}}\right), \\ \rho_{2k+1}^{\text{LC}} &= \rho_{2k-1}^{\text{LC}} + \alpha \rho_{2k}^{\text{LC}} \left(1 - \frac{4}{3} \rho_{2k-1}^{\text{LC}}\right). \end{aligned} \quad (23)$$

Using the first equation, we find

$$\rho_{2k}^{\text{LC}} = 3/4 \quad (24)$$

for any  $k > 0$ . Substituting this into the second equation, we have ( $k \geq 0$ )

$$\rho_{2k+1}^{\text{LC}} = \frac{3}{4} - \left(\frac{3}{4} - \alpha\right) (1 - \alpha)^k. \quad (25)$$

We test both predictions through the Monte Carlo sampling of the  $\rho(x, t)$  at various  $\alpha$  for  $O = Z_0 Z_1$ . Since  $\rho$  becomes spatially independent at  $t \gg 1$ , we focus on the density evolution at  $x=0$  without loss of generality. By fitting the density evolution with Eq. (22), we find an exponential growth coefficient  $\lambda$  that is consistent with the analytical solution in Eq. (22), as shown in Fig. 4. For the near-light-cone steady state, MC data of both  $\rho_{2k}^{\text{LC}}$  and  $\rho_{2k+1}^{\text{LC}}$  exponentially converges to the MF prediction in Eq. (25) at large-enough  $t$ , as exemplified in Fig. 5 (a) and (b) for  $k = 1, 2, 3$  at  $\alpha = 0.2, 0.3, 0.4$ .

### 2. Skewed operator growth from single-site operator

We then consider the operator density evolution for  $O = Z_1$ , as shown in Fig. 3 (b). In this case, the right light-cone ( $x-t=1$ ) has an operator density of 1, while the density on the left light-cone ( $x+t=2$ ) is  $\alpha$ , determined by the probability of operator emission at the first

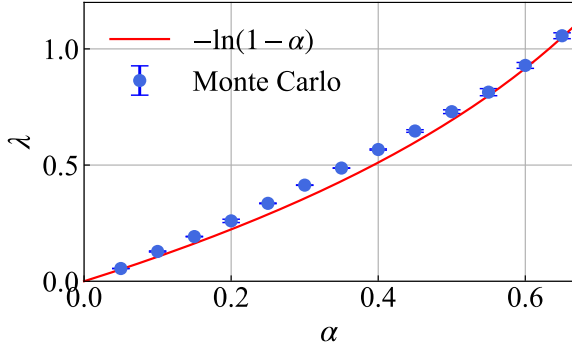


FIG. 4.  $\lambda$  in Eq. (22) as a function of  $\alpha$ . The blue dots are fitted from the MC data of  $\rho(0, t)$  with  $O = Z_0 Z_1$  initial condition. The red solid line denotes the mean-field solution in the long-time limit  $t \gg 1$ .

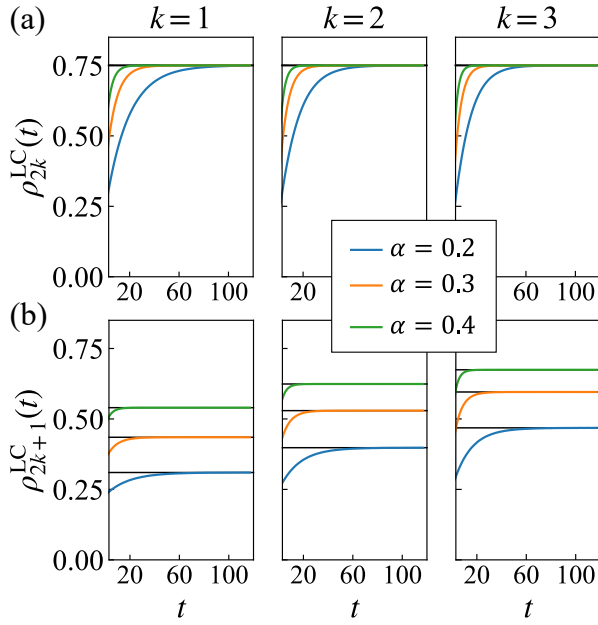


FIG. 5. **Converge of the near-light-cone operator density  $\rho^{\text{LC}}$  obtained from Monte Carlo sampling with  $O = Z_0 Z_1$  initial condition.** Panels (a) and (b) display the density evolution of left movers ( $\rho_{2k}^{\text{LC}}$ ) and right movers ( $\rho_{2k+1}^{\text{LC}}$ ) respectively. Colored lines represent the Monte Carlo data with  $\sim 10^7$  samplings, whereas the horizontal black lines in panels (a) and (b) denote the mean-field result  $\rho_{2k}^{\text{LC}} = 3/4$  and Eq. (25) at corresponding  $k$  values, respectively.

step. Unlike the previous example with  $O = Z_0 Z_1$ , numerical results show that the operator density evolution near the left light-cone differs significantly from a direct mean-field solution. This discrepancy arises because the mean-field analysis is valid only when the operator occupations on different sites are nearly independent, allowing correlations to be neglected. However, strong correlations exist near the left light-cone for  $O = Z_1$ , and this can be explained in the following way.

We consider the conditional probability  $\rho(x, t|t_0)$  of the

full operator dynamics, where  $t_0 = 1, 2, \dots$  labels the time when the initial operator emits a left mover for the first time. This left mover becomes the leftmost particle and will never disappear in subsequent evolution. The probability distribution of  $t_0$  is given by

$$p(t_0) = \alpha(1 - \alpha)^{t_0 - 1}. \quad (26)$$

After the emission of the first left mover, we have two nearest neighbor particles, and the evolution of operator density matches previous discussions for  $O = Z_0 Z_1$ . This results in

$$\rho(x, t | t_0) = \rho(x - t_0, t - t_0)_{ZZ}. \quad (27)$$

Here,  $\rho(x, t)_{ZZ}$  is the operator density for  $O = Z_0 Z_1$ . Specifically, we have  $\rho(x, t|t_0) = 0$  if  $x + t < 2t_0$  and  $\rho(x, t|t_0) = 1$  if  $x + t = 2t_0$ , indicating a long-range correlation between different sites near the left light-cone after summing up contributions from different  $t_0$ . Therefore, a naive mean-field theory does not apply. However, since it has been established that  $\rho(x, t)_{ZZ}$  can be described by the mean-field equation, we can still make predictions using a superposition of mean-field results:

$$\rho(x, t) = \sum_{t_0=1}^{\infty} p(t_0) \rho(x - t_0, t - t_0)_{ZZ}. \quad (28)$$

Since  $p(t_0)$  exponentially localizes at small  $t_0$ , evident from Eq. (26), it does not change the long-time relaxation to  $\rho(x) = 3/4$  and the steady-state operator density near the right light-cone, which is still given by Eq. (25). For the steady-state near the left light-cone, the dependence on  $t_0$  becomes significant. Defining  $\tilde{d} = x + t - 2 \sim O(1)$ , we have  $\tilde{\rho}_0^{\text{LC}} = \alpha$ ,

$$\begin{aligned} \tilde{\rho}_{2k}^{\text{LC}} &= \frac{3}{4} \sum_{t_0=1}^k p(t_0) + p(k+1) \\ &= \frac{3}{4} (1 - (1 - \alpha)^{k-1}) + \alpha(1 - \alpha)^k. \end{aligned} \quad (29)$$

and

$$\begin{aligned} \tilde{\rho}_{2k+1}^{\text{LC}} &= \sum_{t_0=1}^{k+1} p(t_0) \left( \frac{3}{4} - \left( \frac{3}{4} - \alpha \right) (1 - \alpha)^{k+1-t_0} \right) \\ &= \frac{3}{4} - \frac{3}{4} (1 - \alpha)^k \left[ 1 - \alpha \left( \frac{4}{3} \alpha + k \left( -1 + \frac{4}{3} \alpha \right) \right) \right]. \end{aligned} \quad (30)$$

for any  $k > 0$ .

Again, we test the above prediction near the left light-cone with  $O = Z_1$  initial condition by directly comparing with Monte Carlo simulations, as exemplified in Fig. 6 (a) and (b) for  $k = 1, 2, 3$  at  $\alpha = 0.2, 0.3, 0.4$ . The operator density near the left light-cone for both left and right movers converges to the mean-field results in Eqs. (29) and (30) as  $t$  increases.

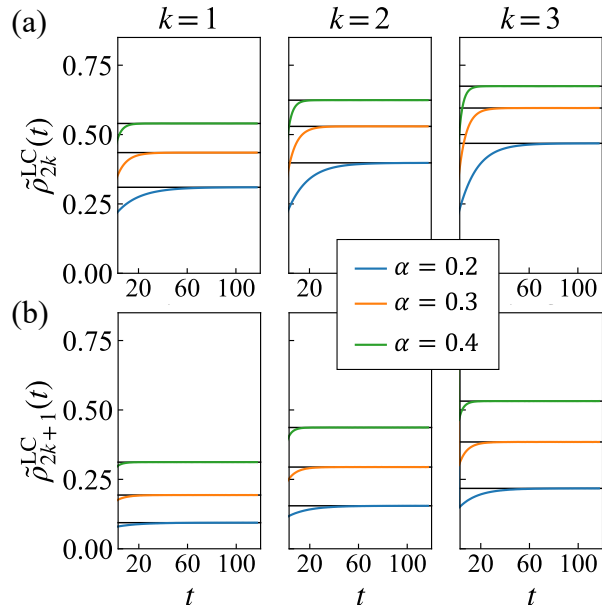


FIG. 6. **Converge of the near-left-light-cone operator density  $\tilde{\rho}^{LC}$  obtained from Monte Carlo sampling with  $O = Z_1$  initial condition.** Panels (a) and (b) display the density evolution of left movers ( $\tilde{\rho}_{2k}^{LC}$ ) and right movers ( $\tilde{\rho}_{2k+1}^{LC}$ ) respectively. Colored lines represent the Monte Carlo data with  $\sim 10^7$  samplings, whereas the horizontal black lines in panels (a) and (b) denote the mean-field results in Eqs. (29) and (30) at corresponding  $k$  values, respectively.

### 3. Summary of results on operator density

In this subsection, we investigated the operator growth dynamics in dual-unitary circuits with a brick-wall arrangement of two-qubit gates, characterized by the gate parameter  $\alpha$ . Near the center of the light cone of the growing operator, the operator density converges exponentially to  $\frac{3}{4}$ , following  $\rho(t) = \frac{3}{4} - Ae^{-\lambda t}$ , with the rate  $\lambda = -\ln(1 - \alpha)$  determined by  $\alpha$ . In the long-time limit, the operator density will converge to the profile depicted in Fig. 7, which oscillates between upper and lower bounds. We derived analytical expressions for these bounds based on a mean-field-like theory, where operators spread like diffusive “particles”, and correlations among these particles are retained only to the minimal necessary order. Their expressions and verifications are summarized in the table within Fig. 7.

## B. Operator Entanglement Growth

Next, we study the dynamics of operator entanglement, focusing on the steady-state entanglement for subregions near the light-cone starting from the single-site operator  $O = Z_1$ . As established in Sec. III A, the results obtained near the right light-cone for  $O = Z_1$  should also apply to both light-cone edges for the two-site operator

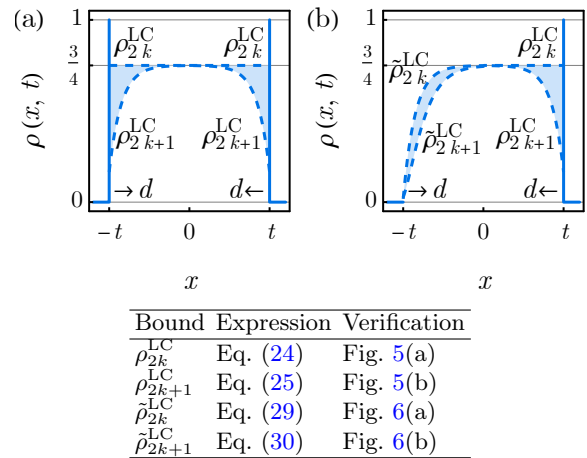


FIG. 7. Schematic plot the operator density distribution  $\rho(x, t)$  in the long-time limit, for operator dynamics starting with (a)  $O = Z_0$  and (b)  $O = Z_0 Z_1$ . The shaded area indicates the operator density oscillates between the upper and lower bounds alternatively. The bounds near the light-cone edge are denoted as  $\rho_d^{LC}$  or  $\tilde{\rho}_d^{LC}$ , with  $d$  being the distance away from the light-cone edge. Their mean-field expressions and verifications with Monte Carlo simulations are summarized in the following table.

$O = Z_0 Z_1$ , so we will not further discuss the operator entanglement dynamics for  $O = Z_0 Z_1$ , and we will focus our discussion on the case of  $O = Z_1$  only. Given the initial operator  $O = Z_1$ , as it evolves under the dual unitary circuit, the operator spreads into a light-cone in the spacetime.

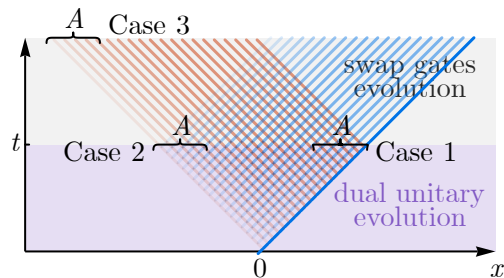


FIG. 8. Illustration of three different choices of the operator entanglement region  $A$  in the spacetime. Assuming a single-site operator at the spacetime origin evolve under dual unitary circuits for sufficiently long time, Cases 1 and 2 concerns the operator entanglement near the two inequivalent light-cone edges. Case 3 consider the operator entanglement of the left movers only, which can be effectively separated from right movers by a subsequent circuit of swap gates.

We consider three different cases with different choices for subregion  $A$  to study the operator entanglement entropy, after evolving  $O = Z_1$  by the dual unitary circuit for time  $t$ , as shown in Fig. 8:



1.  $A$  contains consecutive sites from the right light-cone edge.
2.  $A$  contains consecutive sites from the left light-cone edge.
3.  $A$  contains consecutive left movers from the left light-cone edge.

It worth mention that the Case 3 can be viewed as the operator entanglement on the left light-cone after further evolving the operator by a brick-wall circuit of swap gates (i.e. quenching dual unitary gates to swap gates after time  $t$ ), such that the left- and right-movers are separated. We will be most interested in the scaling of operator entanglement entropy with the region size  $l_A$  in the long-time limit  $t \rightarrow \infty$ , as the operator has been sufficiently scrambled by the dual unitary circuit to exhibit equilibrium behavior.

### 1. Case 1: from the right light-cone edge

We begin with the Case 1, which allows for a direct mean-field description. With the mean-field approximation Eq. (19), we can estimate the  $n$ th Rényi operator entanglement Eq. (15) as

$$\overline{S_{A,1}^{(n)}}(t) \approx -\frac{1}{n-1} \sum_{x \in A} \ln \left( (1 - \rho(x,t))^n + \rho^n(x,t)/3^{n-1} \right). \quad (31)$$

Near the right light-cone, the steady-state operator density, given by Eq. (25), approaches  $\rho = 3/4$  within a length scale of  $-2/\log(1 - \alpha)$ . Therefore, to extract the volume law coefficient of operator entanglement, defined as

$$a_1^{(n)} \equiv \lim_{t \gg l_A \gg 1} \overline{S_A^{(n)}}/l_A,$$

we can safely approximate  $\rho_d^{\text{LC}} = 3/4$ . This leads to the expression  $\overline{S_{A,1}^{(n)}} \approx (2 \ln 2) l_A + O(1)$ , yielding

$$a_1^{(n)} = 2 \ln 2. \quad (32)$$

Since the local operator space has a dimension of 4, this result demonstrates that operator entanglement near the right light-cone is nearly maximal. We demonstrate the maximum growth of the operator entanglement entropy at  $n = 2$ , i.e., second Rényi entropy in Fig. 9. As one can see in Fig. 9 (a), linear scaling of  $\overline{S_{A,1}^{(2)}}$  against the entanglement region  $l_A$  (volume law) is observed only after a long enough evolution time  $t$ , especially at small  $\alpha$  values. The fitted volume law coefficients  $a_1^{(2)}$  against  $\alpha$  at different  $t$  are presented in Fig. 9 (b). At large  $\alpha$ ,  $a_1^{(2)}$  is found to be maximum  $2 \ln 2$ , even at small  $t$ . However,  $a_1^{(2)}$  drifts drastically against  $t$  at small  $\alpha$ . Therefore, we extrapolate the  $t \rightarrow \infty$  limit from finite- $t$   $a_1^{(2)}$  values,

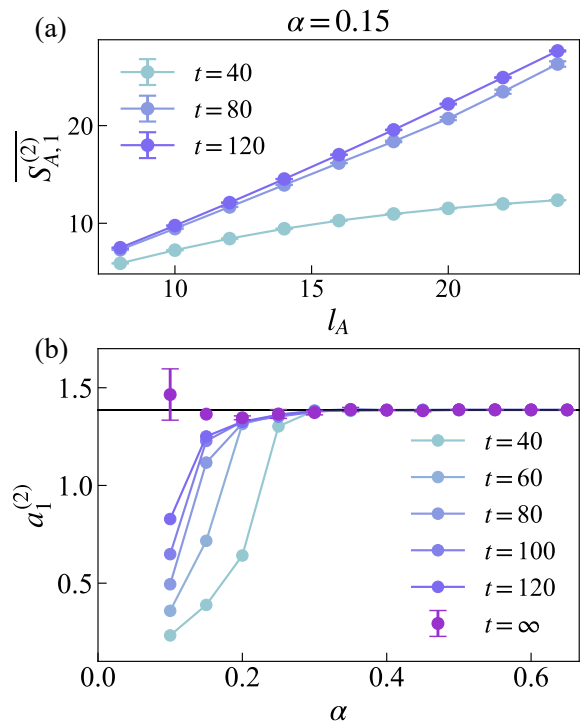


FIG. 9. **Scaling the operator entanglement entropy for Case 1.** (a) The linear growth of the operator entanglement entropy with respect to the entanglement region length  $l_A$  at  $\alpha = 0.15$  as an example. Notice that the evolution time at small  $\alpha$  should be long enough to manifest the linear growth. (b) The fitted leading volume law coefficient as a function of  $\alpha$  obtained at various evolution times  $t$ .  $a_1^{(2)}$  values at  $t = \infty$  are extrapolated from the finite- $t$  results at each  $\alpha$  with a power-law fitting. The horizontal black line represents the maximal growth speed  $2 \ln 2$ . The entanglement entropy data is averaged over  $\sim 10^8$  samplings.

denoted as the purple dots with error bars in Fig. 9 (b). The extrapolated values demonstrate a maximum growth of the operator entanglement entropy for all  $\alpha \in [0, 2/3]$  at  $t \rightarrow \infty$ , consistent with the mean-field analysis above.

### 2. Case 2: from the left light-cone edge

Now, let us consider Case 2 near the left light-cone. Similar to the calculation of the operator density, we introduce the conditional joint distribution function  $w_{P_A}(t|t_0)$  given an emission of a left-mover for the first time at  $t_0$  and express the reduced density matrix as follows:

$$\overline{\rho_A} = \sum_{t_0} p(t_0) \sum_{P_A^{(t_0)}} w_{P_A^{(t_0)}}(t|t_0) |P_A^{(t_0)}\rangle \langle P_A^{(t_0)}|. \quad (33)$$

Here,  $w_{P_A}(t|t_0)$  matches the joint distribution with the initial operator  $O = Z_0 Z_1$ , with shifted space-time indices. An important observation is that  $t_0$  determines

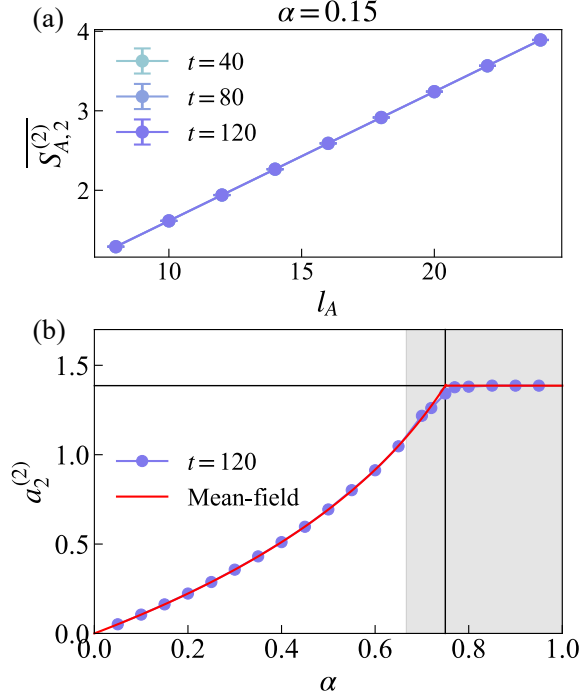


FIG. 10. **Scaling the operator entanglement entropy for Case 2.** (a) The fitted linear growth of the operator entanglement entropy with respect to the entanglement region length  $l_A$  at  $\alpha = 0.15$  as an example. The operator entanglement entropy measured at different times is nearly identical such that the markers overlap with each other. (b) The leading volume law coefficient as a function of  $\alpha$  obtained at various evolution times  $t = 120$ . A transition between a maximal and a sub-maximal growth of the entanglement entropy manifests. The horizontal black line represents the maximal growth speed  $2 \ln 2$ , whereas the vertical one indicates the transition point  $\alpha = 3/4$ . The shaded area marks the unphysical region where  $\alpha$  exceeds  $2/3$ . The entanglement entropy data computed by averaging over  $\sim 10^8$  samples.

the position of the leftmost particle. Therefore, for  $t_0, t'_0 \leq (l_A + 1)/2$  and  $t_0 \neq t'_0$ , we have  $\langle P_A^{(t_0)} | P_A^{(t'_0)} \rangle = 0$ . On the other hand, for  $t_0 > (l_A + 1)/2$ , the subsystem  $A$  contains only the identity operator  $|I\rangle$ . Consequently, we can rewrite the reduced density matrix as

$$\begin{aligned} \bar{\rho}_A = & \sum_{t_0 \leq \frac{l_A+1}{2}} p(t_0) \sum_{P_A^{(t_0)}} w_{P_A^{(t_0)}}(t|t_0) |P_A^{(t_0)}\rangle \langle P_A^{(t_0)}| \\ & + \sum_{t_0 > \frac{l_A+1}{2}} p(t_0) |I\rangle. \end{aligned} \quad (34)$$

Here, all different terms are orthogonal. Taking the mean-field approximation for the conditional distribution, we can express the operator entanglement entropy

as

$$\begin{aligned} e^{-(n-1)\overline{S_{A,2}^{(n)}}} = & \sum_{1 \leq t_0 \leq \frac{l_A+1}{2}} p^n(t_0) e^{-(n-1)\overline{S_{A,1}^{(n)}}} \\ & + \left( \sum_{t_0 > \frac{l_A+1}{2}} p(t_0) \right)^n. \end{aligned} \quad (35)$$

In this equation, we have identified the contribution from  $\sum_{P_A^{(t_0)}} w_{P_A^{(t_0)}}(t|t_0) |P_A^{(t_0)}\rangle \langle P_A^{(t_0)}|$  as the operator entanglement of a subsystem  $\tilde{A}$ , which contains  $l_A - 2t_0 + 2$  sites near the left light-cone for the initial operator  $O = Z_0 Z_1$ . The corresponding result matches the findings of Case 1 for  $O = Z_1$ .

To extract the volume-law coefficient, we use  $\overline{S_{A,1}^{(n)}} \approx (l_A - 2t_0 + 2) \times 2 \ln 2$ . Moreover, for large  $l_A$ , we can neglect the last term in Eq. (35). The result reads

$$e^{-(n-1)\overline{S_{A,2}^{(n)}}} = \alpha^n \sum_{1 \leq t_0 \leq \frac{l_A+1}{2}} (1-\alpha)^{n(t_0-1)} 4^{-(n-1)(l_A-2t_0+2)}. \quad (36)$$

Instead of a direct calculation of the summation, we can estimate by extracting the  $t_0$  dependence, which scales as  $\beta^{t_0}$  with  $\beta := 2^{4(n-1)}(1-\alpha)^n$ . When we have  $\beta > 1$ , the dominant contribution is from  $t_0 \approx (l_A + 1)/2$ , while for  $\beta < 1$ , the dominant contribution comes from  $t_0 \approx 0$ . Therefore, we have

$$a_2^{(n)} = \begin{cases} -\frac{n}{2(n-1)} \ln(1-\alpha) & \text{if } \alpha < 1 - 2^{-\frac{4(n-1)}{n}}, \\ 2 \ln 2 & \text{if } \alpha > 1 - 2^{-\frac{4(n-1)}{n}}. \end{cases} \quad (37)$$

This suggests a possible transition in operator entanglement as we tune  $\alpha$ . Unfortunately, since the mapping from the original quantum circuits to the Markovian process requires  $\alpha \leq 2/3$ , the transition point  $\alpha_c = 1 - 2^{-\frac{4(n-1)}{n}}$  is never accessible for integers  $n \geq 2$ . On the other hand, taking the limit  $n = 1$  leads to  $\alpha_c = 0$ . A non-trivial entanglement transition at finite  $\alpha$  only exist for  $1 < n < (1 - (\log_2 3)/4)^{-1} \approx 1.66$ .

From Eq. (37), the transition for the second Rényi entanglement,  $n = 2$  appears at  $\alpha_c = 3/4$ . Although  $\alpha = 3/4$  is out of the legitimate domain of the dual unitary gate parameter, we can nonetheless perform Monte Carlo sampling in the entire range  $\alpha \in [0, 1]$ . Fig. 10 (a) demonstrates the volume law growth of the entanglement entropy. In this case, entanglement entropy converges very quickly against the evolution time  $t$  such that the data measured at  $t = 40$  is almost identical to that measured at  $t = 120$ , in contrast to the strong time-dependent feature observed in Case 1. A transition at  $\alpha_c = 3/4$  is successfully detected by the volume law coefficient  $a_2^{(2)}$ : below  $\alpha = 3/4$ ,  $a_2^{(2)}$  increases as  $-\ln(1-\alpha)$  consistent with mean-field analysis and remains the maximum value when  $\alpha > 3/4$ .

3. Case 3: from the left light-cone edge, focusing on left-movers only

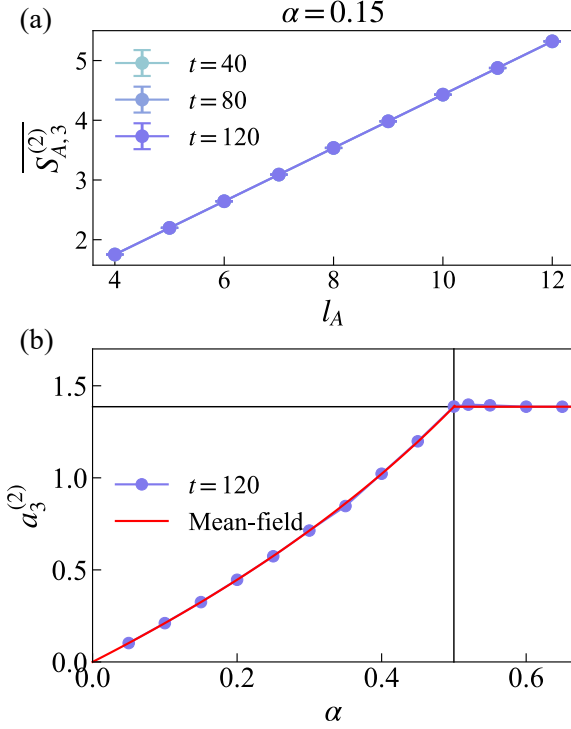


FIG. 11. **Scaling the operator entanglement entropy for Case 3.** (a) The linear growth of the operator entanglement entropy with respect to the entanglement region containing only left-movers at  $\alpha = 0.15$  as an example. The operator entanglement entropy measured at different times is nearly identical such that the markers overlap with each other. (b) The fitted leading volume law coefficient as a function of  $\alpha$  obtained at various evolution times  $t = 120$ . A transition between a maximal and a sub-maximal growth of the entanglement entropy manifests. The horizontal black line represents the maximal growth speed  $2 \ln 2$ , whereas the vertical one indicates the transition point  $\alpha = 1/2$ . The entanglement entropy data is averaged over  $\sim 10^8$  samplings.

We can construct a scenario where an entanglement transition can be observed at a finite  $\alpha$  within the physical range of the gate parameter. This is described in Case 3, where we consider only the subsystem  $A$  of left movers. Following the analysis of Case 2, the only difference is a reduction of  $\overline{S_{A,1}^{(n)}}$  by a factor of two. Therefore, we expect

$$e^{-(n-1)\overline{S_{A,3}^{(n)}}} \approx \alpha^n \sum_{1 \leq t_0 \leq l_A+1} (1-\alpha)^{n(t_0-1)} 4^{-(n-1)(l_A-t_0+1)}. \quad (38)$$

This results in a change in the critical  $\alpha$ :

$$a_3^{(n)} = \begin{cases} -\frac{n}{n-1} \ln(1-\alpha) & \text{if } \alpha < 1 - 2^{-\frac{2(n-1)}{n}}, \\ 2 \ln 2 & \text{if } \alpha > 1 - 2^{-\frac{2(n-1)}{n}}. \end{cases} \quad (39)$$

An entanglement transition exists for  $1 < n < (1 - (\log_2 3)/2)^{-1} \approx 4.82$ . In particular, we find  $\alpha_c = 1/2$  for the second Rényi operator entanglement, which is also verified via numerical simulation in Fig. 11 (b). The growing behavior of  $a_3^{(2)}$  at the sub-maximal growth region, i.e.,  $\alpha < 1/2$ , also agrees with the mean-field prediction, which reads  $-2 \ln(1-\alpha)$  at  $n = 2$ .

4. Summary of results on operator entanglement

In this subsection, we studied the dynamics of operator entanglement in dual-unitary circuits, examining three distinct cases based on different subregions near the light-cone with the initial operator  $O = Z_1$ , as illustrated in Fig. 8. Across all three cases, the  $n$ th-Rényi operator entanglement entropy  $\overline{S_A^{(n)}}(t)$ , as defined in Eq. (13), exhibits a volume-law scaling on both edges of the light cone in the long-time limit  $t \rightarrow \infty$ , i.e.

$$\overline{S_A^{(n)}} \simeq a^{(n)} l_A + \dots, \quad (40)$$

growing linearly with the subregion size  $l_A$ . However, the dependence of the volume-law coefficient  $a^{(n)}$  on the gate parameter  $\alpha$  and the Rényi index  $n$  differs between the cases, as summarized in Fig. 12.

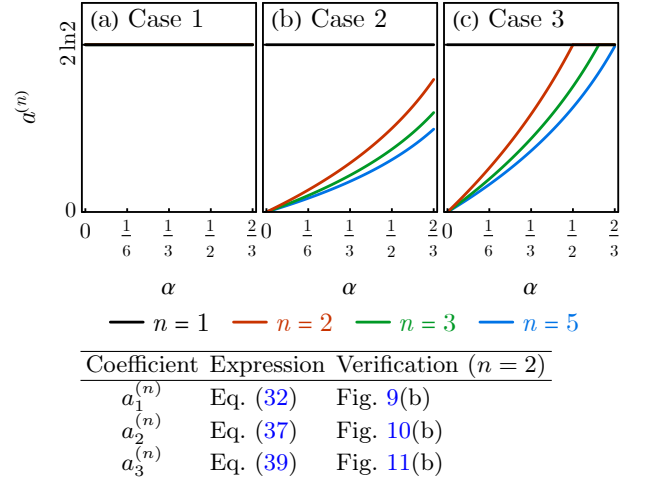


FIG. 12. Summary of the volume-law coefficient  $a^{(n)}$  of the  $n$ th-Rényi operator entanglement entropy, depending on the dual unitary gate parameter  $\alpha$  for three cases of entanglement regions: (a) from the right light-cone edge, (b) from the left light-cone edge, (c) from the left light-cone edge focusing on left-movers only. Maximal to sub-maximal volume-law transition in operator entanglement only happens in the last case.

The transition from maximal to sub-maximal volume-law growth in operator entanglement is observed specifically in Case 3, when focusing on the left movers in the left light-cone entanglement region. This result highlights how the gate parameter  $\alpha$  influence the degree of operator entanglement among the leading left movers

emitted from the expanding operator. Such operator entanglement transitions, characterized by the abrupt drop in the volume-law coefficient at a critical value of  $\alpha$ , have been previously discussed in the literature [35, 36, 39]. Notably, Ref. [36] first identified the operator entanglement transition in a setup akin to our Case 2 and derived the following formula for qubit systems:

$$a^{(n)} = \begin{cases} -\frac{n}{n-1} \ln |\lambda|^2 & \text{if } 1 > |\lambda|^2 > 2^{-\frac{2(n-1)}{n}}, \\ 2 \ln 2 & \text{otherwise,} \end{cases} \quad (41)$$

where  $\lambda$  is the leading non-trivial eigenvalue of a transfer matrix defined therein. However, the explicit dependence of  $\lambda$  on the gate parameter was not fully established. Our study builds upon this foundation by demonstrating that this behavior actually aligns precisely with our Case 3 scenario when we identify  $|\lambda|^2 = 1 - \alpha = 1 - \frac{2}{3} \cos^2(2J)$ .

As a result, we clarify the appropriate entanglement region setup necessary to observe the operator entanglement transition in dual-unitary circuits, providing a mean-field formula for the volume-law coefficient directly in terms of the gate parameter. This result is supported by Monte Carlo simulations, which show excellent agreement with our theoretical predictions.

#### IV. DISCUSSION

In this manuscript, we systematically investigate the operator density evolution and entanglement entropy scaling in dual-unitary circuits by mapping the dynamics to a classical Markov process, enabling efficient Monte Carlo simulations. For operator density, we demonstrate that near the center of the light cone, the operator density converges exponentially to a steady value of  $\frac{3}{4}$ , with a rate governed by the gate parameter  $\alpha$ . In the long-time limit, we derive analytical expressions for the operator density profile's upper and lower bounds, which are verified through simulations.

For operator entanglement, we analyze three distinct subregions near the light cone and find that the operator entanglement entropy consistently follows a volume-law scaling. However, the volume-law coefficient's dependence on  $\alpha$  differs across cases. Notably, we identify a transition from maximal to sub-maximal volume-law growth when focusing on left movers near the left light cone. This transition, characterized by a sudden drop in the volume-law coefficient at a critical  $\alpha$ , aligns with prior theoretical predictions in the literature [35, 36, 39]. Additionally, we extend this understanding by providing a direct mapping of the volume-law coefficient to the gate parameter, supported by mean-field theory and validated through Monte Carlo simulations. Our work not

only clarifies the conditions under which operator entanglement transitions occur but also offers a comprehensive framework for studying operator dynamics and entanglement in dual-unitary circuits.

Our result could have implications in *classical shadow tomography* [55] and can be extended to random quantum circuits with symmetries. Classical shadow tomography is a recently developed method for efficiently predicting many properties of quantum systems using a limited number of measurements [55–58]. By understanding operator dynamics and entanglement growth, we can improve the efficiency of classical shadow protocols, leading to more accurate reconstructions of quantum states and observables in many-body systems [59–85]. More specifically, the advantage of using dual unitary circuit in classical shadow tomography has been recently discussed in Ref. [40].

An interesting future direction is to extend our stochastic simulation framework to random quantum circuits with symmetries, which play a crucial role in modeling realistic quantum systems that conserve quantities such as particle number or spin [5, 86–91]. Incorporating symmetries into operator dynamics affects the spreading and entanglement properties, offering deeper insights into the role of conserved quantities in quantum information scrambling and thermalization. Our approach provides a pathway to study these effects efficiently, bridging the gap between solvable models and more complex, realistic systems.

#### ACKNOWLEDGMENTS

*Acknowledgments*— We thank Yimu Bao, Tian-Gang Zhou for discussions. MHS, TTW and ZYM acknowledge the support from the Research Grants Council (RGC) of Hong Kong (Project Nos. 17301721, AoE/P-701/20, 17309822, HKU C7037-22GF, 17302223, 17301924), the ANR/RGC Joint Research Scheme sponsored by RGC of Hong Kong and French National Research Agency (Project No. A\_HKU703/22), the GD-NSF (No. 2022A1515011007). PZ acknowledges the support from the National Natural Science Foundation of China under Grant No. 12374477. YZY is supported by a startup fund from UCSD. We thank HPC2021 system under the Information Technology Services, The University of Hong Kong, as well as the Beijing PARATERA Tech CO.,Ltd. (URL: <https://cloud.paratera.com>) for providing HPC resources that have contributed to the research results reported within this paper. ZYZ, YZY and ZYM acknowledge the hospitality of Kavli Institute for Theoretical Physics (KITP) and thank the organizers of the KITP program “Correlated Gapless Quantum Matter” where this work was initiated. This research was supported in part by grant NSF PHY-2309135 to the KITP.



- 
- [1] W. W. Ho and D. A. Abanin, Entanglement dynamics in quantum many-body systems, *Phys. Rev. B* **95**, 094302 (2017).
- [2] A. Nahum, J. Ruhman, S. Vijay, and J. Haah, Quantum Entanglement Growth under Random Unitary Dynamics, *Physical Review X* **7**, 031016 (2017).
- [3] A. Nahum, S. Vijay, and J. Haah, Operator Spreading in Random Unitary Circuits, *Physical Review X* **8**, 021014 (2018).
- [4] C. W. von Keyserlingk, T. Rakovszky, F. Pollmann, and S. L. Sondhi, Operator Hydrodynamics, OTOCs, and Entanglement Growth in Systems without Conservation Laws, *Physical Review X* **8**, 021013 (2018).
- [5] V. Khemani, A. Vishwanath, and D. A. Huse, Operator Spreading and the Emergence of Dissipative Hydrodynamics under Unitary Evolution with Conservation Laws, *Physical Review X* **8**, 031057 (2018).
- [6] A. Chan, A. De Luca, and J. T. Chalker, Solution of a Minimal Model for Many-Body Quantum Chaos, *Physical Review X* **8**, 041019 (2018).
- [7] T. Zhou and X. Chen, Operator dynamics in a Brownian quantum circuit, *Phys. Rev. E* **99**, 052212 (2019).
- [8] X.-L. Qi, E. J. Davis, A. Periwai, and M. Schleier-Smith, Measuring operator size growth in quantum quench experiments, *arXiv e-prints*, [arXiv:1906.00524](https://arxiv.org/abs/1906.00524) (2019).
- [9] C. von Keyserlingk, F. Pollmann, and T. Rakovszky, Operator backflow and the classical simulation of quantum transport, *Phys. Rev. B* **105**, 245101 (2022).
- [10] T. Schuster and N. Y. Yao, Operator Growth in Open Quantum Systems, *arXiv e-prints*, [arXiv:2208.12272](https://arxiv.org/abs/2208.12272) (2022).
- [11] A. Bohrdt, C. B. Mendl, M. Endres, and M. Knap, Scrambling and thermalization in a diffusive quantum many-body system, *New Journal of Physics* **19**, 063001 (2017).
- [12] I. Kukuljan, S. Grozdanov, and T. Prosen, Weak quantum chaos, *Phys. Rev. B* **96**, 060301 (2017).
- [13] S. Xu and B. Swingle, Locality, Quantum Fluctuations, and Scrambling, *Physical Review X* **9**, 031048 (2019).
- [14] D. E. Parker, X. Cao, A. Avdoshkin, T. Scaffidi, and E. Altman, A Universal Operator Growth Hypothesis, *Physical Review X* **9**, 041017 (2019).
- [15] W.-T. Kuo, A. A. Akhtar, D. P. Arovas, and Y.-Z. You, Markovian entanglement dynamics under locally scrambled quantum evolution, *Phys. Rev. B* **101**, 224202 (2020).
- [16] A. A. Akhtar and Y.-Z. You, Multiregion entanglement in locally scrambled quantum dynamics, *Phys. Rev. B* **102**, 134203 (2020).
- [17] R. Zhang and H. Zhai, Universal Hypothesis of Autocorrelation Function from Krylov Complexity, *arXiv e-prints*, [arXiv:2305.02356](https://arxiv.org/abs/2305.02356) (2023).
- [18] C. Liu, H. Tang, and H. Zhai, Krylov complexity in open quantum systems, *Physical Review Research* **5**, 033085 (2023).
- [19] B. Buča, Unified Theory of Local Quantum Many-Body Dynamics: Eigenoperator Thermalization Theorems, *Physical Review X* **13**, 031013 (2023).
- [20] P. Zhang and Y. Gu, Operator size distribution in large  $N$  quantum mechanics of Majorana fermions, *JHEP* (10) 018.
- [21] P. Zhang and Z. Yu, Dynamical Transition of Operator Size Growth in Quantum Systems Embedded in an Environment, *Phys. Rev. Lett.* **130**, 250401 (2023).
- [22] D. Gottesman, The Heisenberg Representation of Quantum Computers, *arXiv e-prints*, [quant-ph/9807006](https://arxiv.org/abs/quant-ph/9807006) (1998).
- [23] G. Vidal, Efficient Simulation of One-Dimensional Quantum Many-Body Systems, *Phys. Rev. Lett.* **93**, 040502 (2004).
- [24] J. Haegeman, J. I. Cirac, T. J. Osborne, I. Pižorn, H. Verschelde, and F. Verstraete, Time-Dependent Variational Principle for Quantum Lattices, *Phys. Rev. Lett.* **107**, 070601 (2011).
- [25] J. Haegeman, C. Lubich, I. Oseledets, B. Vandereycken, and F. Verstraete, Unifying time evolution and optimization with matrix product states, *Phys. Rev. B* **94**, 165116 (2016).
- [26] D. Muth, R. G. Unanyan, and M. Fleischhauer, Dynamical Simulation of Integrable and Nonintegrable Models in the Heisenberg Picture, *Phys. Rev. Lett.* **106**, 077202 (2011).
- [27] V. Alba, J. Dubail, and M. Medenjak, Operator Entanglement in Interacting Integrable Quantum Systems: The Case of the Rule 54 Chain, *Phys. Rev. Lett.* **122**, 250603 (2019).
- [28] C. Jonay, D. A. Huse, and A. Nahum, Coarse-grained dynamics of operator and state entanglement, *arXiv e-prints*, [arXiv:1803.00089](https://arxiv.org/abs/1803.00089) (2018).
- [29] T. Zhou and A. Nahum, Emergent statistical mechanics of entanglement in random unitary circuits, *Phys. Rev. B* **99**, 174205 (2019).
- [30] C. de Groot, A. Turzillo, and N. Schuch, Symmetry Protected Topological Order in Open Quantum Systems, *Quantum* **6**, 856 (2022).
- [31] R. Ma and C. Wang, Average Symmetry-Protected Topological Phases, *Physical Review X* **13**, 031016 (2023).
- [32] A. Nahum, S. Roy, S. Vijay, and T. Zhou, Real-time correlators in chaotic quantum many-body systems, *Phys. Rev. B* **106**, 224310 (2022).
- [33] L. Nie, M. Nozaki, S. Ryu, and M. Tian Tan, Signature of quantum chaos in operator entanglement in 2d CFTs, *Journal of Statistical Mechanics: Theory and Experiment* **9**, 093107 (2019).
- [34] J. Kudler-Flam, M. Nozaki, S. Ryu, and M. T. Tan, Quantum vs. classical information: operator negativity as a probe of scrambling, *Journal of High Energy Physics* **2020**, 31 (2020).
- [35] B. Bertini, P. Kos, and T. Prosen, Operator Entanglement in Local Quantum Circuits II: Solitons in Chains of Qubits, *SciPost Phys.* **8**, 068 (2020).
- [36] B. Bertini, P. Kos, and T. Prosen, Operator Entanglement in Local Quantum Circuits I: Chaotic Dual-Unitary Circuits, *SciPost Phys.* **8**, 067 (2020).
- [37] A. Jamiolkowski, Linear transformations which preserve trace and positive semidefiniteness of operators, *Reports on Mathematical Physics* **3**, 275 (1972).
- [38] M.-D. Choi, Completely positive linear maps on complex matrices, *Linear Algebra and its Applications* **10**, 285 (1975).
- [39] B. Bertini, P. Kos, and T. c. v. Prosen, Exact Correlation Functions for Dual-Unitary Lattice Models in  $1 + 1$

- Dimensions, *Phys. Rev. Lett.* **123**, 210601 (2019).
- [40] A. A. Akhtar, N. Anand, J. Marshall, and Y.-Z. You, Dual-Unitary Classical Shadow Tomography, *arXiv e-prints*, [arXiv:2404.01068](https://arxiv.org/abs/2404.01068) (2024).
- [41] A. Hamma, S. Santra, and P. Zanardi, Quantum Entanglement in Random Physical States, *Phys. Rev. Lett.* **109**, 040502 (2012).
- [42] P. Hayden, S. Nezami, X.-L. Qi, N. Thomas, M. Walter, and Z. Yang, Holographic duality from random tensor networks, *Journal of High Energy Physics* **2016**, 9 (2016).
- [43] Y. Da Liao, Controllable Incremental Algorithm for Entanglement Entropy in Quantum Monte Carlo Simulations, *arXiv e-prints*, [arXiv:2307.10602](https://arxiv.org/abs/2307.10602) (2023).
- [44] X. Zhang, G. Pan, B.-B. Chen, K. Sun, and Z. Y. Meng, Integral algorithm of exponential observables for interacting fermions in quantum Monte Carlo simulations, *Phys. Rev. B* **109**, 205147 (2024).
- [45] X. Zhou, Z. Y. Meng, Y. Qi, and Y. Da Liao, Incremental SWAP operator for entanglement entropy: Application for exponential observables in quantum Monte Carlo simulation, *Phys. Rev. B* **109**, 165106 (2024).
- [46] M. B. Hastings, I. González, A. B. Kallin, and R. G. Melko, Measuring Rényi Entanglement Entropy in Quantum Monte Carlo Simulations, *Phys. Rev. Lett.* **104**, 157201 (2010).
- [47] D. J. Luitz, X. Plat, N. Laflorencie, and F. Alet, Improving entanglement and thermodynamic Rényi entropy measurements in quantum Monte Carlo, *Phys. Rev. B* **90**, 125105 (2014).
- [48] M. Song, T.-T. Wang, and Z. Y. Meng, Resummation-based quantum Monte Carlo for entanglement entropy computation, *Phys. Rev. B* **110**, 115117 (2024).
- [49] J. D’Emidio, Entanglement Entropy from Nonequilibrium Work, *Phys. Rev. Lett.* **124**, 110602 (2020).
- [50] J. Zhao, Y.-C. Wang, Z. Yan, M. Cheng, and Z. Y. Meng, Scaling of Entanglement Entropy at Deconfined Quantum Criticality, *Phys. Rev. Lett.* **128**, 010601 (2022).
- [51] J. Zhao, B.-B. Chen, Y.-C. Wang, Z. Yan, M. Cheng, and Z. Y. Meng, Measuring Rényi entanglement entropy with high efficiency and precision in quantum Monte Carlo simulations, *npj Quantum Materials* **7**, 69 (2022).
- [52] M. Song, J. Zhao, Z. Y. Meng, C. Xu, and M. Cheng, Extracting subleading corrections in entanglement entropy at quantum phase transitions, *SciPost Phys.* **17**, 010 (2024).
- [53] T.-T. Wang, M. Song, Z. Y. Meng, and T. Grover, An analog of topological entanglement entropy for mixed states, *arXiv e-prints*, [arXiv:2407.20500](https://arxiv.org/abs/2407.20500) (2024).
- [54] M. Ippoliti, Y. Li, T. Rakovszky, and V. Khemani, Operator Relaxation and the Optimal Depth of Classical Shadows, *Phys. Rev. Lett.* **130**, 230403 (2023).
- [55] H.-Y. Huang, R. Kueng, and J. Preskill, Predicting many properties of a quantum system from very few measurements, *Nature Physics* **16**, 1050 (2020).
- [56] M. Ohliger, V. Nesme, and J. Eisert, Efficient and feasible state tomography of quantum many-body systems, *New Journal of Physics* **15**, 015024 (2013).
- [57] M. Guta, J. Kahn, R. Kueng, and J. A. Tropp, Fast state tomography with optimal error bounds, *Journal of Physics A: Mathematical and Theoretical* **53**, 204001 (2020).
- [58] A. Elben, R. Kueng, H.-Y. R. Huang, R. van Bijnen, C. Kokail, M. Dalmonte, P. Calabrese, B. Kraus, J. Preskill, P. Zoller, and B. Vermersch, Mixed-State Entanglement from Local Randomized Measurements, *Phys. Rev. Lett.* **125**, 200501 (2020).
- [59] H.-Y. Huang, M. Broughton, M. Mohseni, R. Babbush, S. Boixo, H. Neven, and J. R. McClean, Power of data in quantum machine learning, *Nature Communications* **12**, 2631 (2021).
- [60] H.-Y. Huang, R. Kueng, and J. Preskill, Information-Theoretic Bounds on Quantum Advantage in Machine Learning, *Phys. Rev. Lett.* **126**, 190505 (2021).
- [61] H.-Y. Huang, R. Kueng, G. Torlai, V. V. Albert, and J. Preskill, Provably efficient machine learning for quantum many-body problems, *arXiv e-prints*, [arXiv:2106.12627](https://arxiv.org/abs/2106.12627) (2021).
- [62] H.-Y. Huang, R. Kueng, and J. Preskill, Efficient Estimation of Pauli Observables by Derandomization, *Phys. Rev. Lett.* **127**, 030503 (2021).
- [63] R. Levy, D. Luo, and B. K. Clark, Classical Shadows for Quantum Process Tomography on Near-term Quantum Computers, *arXiv e-prints*, [arXiv:2110.02965](https://arxiv.org/abs/2110.02965) (2021).
- [64] A. Acharya, S. Saha, and A. M. Sengupta, Shadow tomography based on informationally complete positive operator-valued measure, *Phys. Rev. A* **104**, 052418 (2021).
- [65] H.-Y. Hu and Y.-Z. You, Hamiltonian-driven shadow tomography of quantum states, *Physical Review Research* **4**, 013054 (2022).
- [66] K. Bu, D. Enshan Koh, R. J. Garcia, and A. Jaffe, Classical shadows with Pauli-invariant unitary ensembles, *arXiv e-prints*, [arXiv:2202.03272](https://arxiv.org/abs/2202.03272) (2022).
- [67] A. Seif, Z.-P. Cian, S. Zhou, S. Chen, and L. Jiang, Shadow Distillation: Quantum Error Mitigation with Classical Shadows for Near-Term Quantum Processors, *arXiv e-prints*, [arXiv:2203.07309](https://arxiv.org/abs/2203.07309) (2022).
- [68] H.-Y. Hu, R. LaRose, Y.-Z. You, E. Rieffel, and Z. Wang, Logical shadow tomography: Efficient estimation of error-mitigated observables, *arXiv e-prints*, [arXiv:2203.07263](https://arxiv.org/abs/2203.07263) (2022).
- [69] H. Chau Nguyen, J. Lennart Bönsel, J. Steinberg, and O. Gühne, Optimising shadow tomography with generalised measurements, *arXiv e-prints*, [arXiv:2205.08990](https://arxiv.org/abs/2205.08990) (2022).
- [70] C. Hadfield, S. Bravyi, R. Raymond, and A. Mezzacapo, Measurements of Quantum Hamiltonians with Locally-Biased Classical Shadows, *Communications in Mathematical Physics* **391**, [arXiv:2006.15788](https://arxiv.org/abs/2006.15788) (2022).
- [71] H.-Y. Huang, M. Broughton, J. Cotler, S. Chen, J. Li, M. Mohseni, H. Neven, R. Babbush, R. Kueng, J. Preskill, and J. R. McClean, Quantum advantage in learning from experiments, *Science* **376**, 1182 (2022).
- [72] D. Enshan Koh and S. Grewal, Classical Shadows With Noise, *Quantum* **6**, [arXiv:2011.11580](https://arxiv.org/abs/2011.11580) (2022).
- [73] G. Hao Low, Classical shadows of fermions with particle number symmetry, *arXiv e-prints*, [arXiv:2208.08964](https://arxiv.org/abs/2208.08964) (2022).
- [74] C. Bertoni, J. Haferkamp, M. Hinsche, M. Ioannou, J. Eisert, and H. Pashayan, Shallow shadows: Expectation estimation using low-depth random Clifford circuits, *arXiv e-prints*, [arXiv:2209.12924](https://arxiv.org/abs/2209.12924) (2022).
- [75] M. Arienzo, M. Heinrich, I. Roth, and M. Kliesch, Closed-form analytic expressions for shadow estimation with brickwork circuits, *arXiv e-prints*, [arXiv:2211.09835](https://arxiv.org/abs/2211.09835) (2022).
- [76] H.-Y. Hu, S. Choi, and Y.-Z. You, Classical Shadow Tomography with Locally Scrambled Quantum Dynamics,

- Physical Review Research **5**, arXiv:2107.04817 (2023).
- [77] A. A. Akhtar, H.-Y. Hu, and Y.-Z. You, Scalable and Flexible Classical Shadow Tomography with Tensor Networks, *Quantum* **7**, 1026 (2023).
- [78] S. Zhang, X. Feng, M. Ippoliti, and Y.-Z. You, Holographic Classical Shadow Tomography, arXiv e-prints , arXiv:2406.11788 (2024).
- [79] A. A. Akhtar, H.-Y. Hu, and Y.-Z. You, Measurement-induced criticality is tomographically optimal, *Phys. Rev. B* **109**, 094209 (2024).
- [80] H.-Y. Hu, A. Gu, S. Majumder, H. Ren, Y. Zhang, D. S. Wang, Y.-Z. You, Z. Mineev, S. F. Yelin, and A. Seif, Demonstration of Robust and Efficient Quantum Property Learning with Shallow Shadows, arXiv e-prints , arXiv:2402.17911 (2024).
- [81] Z. Liu, Z. Hao, and H.-Y. Hu, Predicting Arbitrary State Properties from Single Hamiltonian Quench Dynamics, arXiv e-prints , arXiv:2311.00695 (2023).
- [82] Y. Shen, A. Buzali, H.-Y. Hu, K. Klymko, D. Camps, S. F. Yelin, and R. Van Beeumen, Efficient Measurement-Driven Eigenenergy Estimation with Classical Shadows, arXiv e-prints , arXiv:2409.13691 (2024).
- [83] M. Ippoliti and V. Khemani, Learnability Transitions in Monitored Quantum Dynamics via Eavesdropper's Classical Shadows, *PRX Quantum* **5**, 020304 (2024).
- [84] M. Ippoliti, Classical shadows based on locally-entangled measurements, *Quantum* **8**, 1293 (2024).
- [85] S. Chen, W. Gong, and Q. Ye, Optimal trade-offs for estimating Pauli observables, arXiv e-prints , arXiv:2404.19105 (2024).
- [86] T. Rakovszky, F. Pollmann, and C. W. von Keyserlingk, Diffusive Hydrodynamics of Out-of-Time-Ordered Correlators with Charge Conservation, *Physical Review X* **8**, 031058 (2018).
- [87] N. Hunter-Jones, Operator growth in random quantum circuits with symmetry, arXiv e-prints , arXiv:1812.08219 (2018).
- [88] U. Agrawal, A. Zabalo, K. Chen, J. H. Wilson, A. C. Potter, J. H. Pixley, S. Gopalakrishnan, and R. Vasseur, Entanglement and Charge-Sharpener Transitions in U(1) Symmetric Monitored Quantum Circuits, *Phys. Rev. X* **12**, 041002 (2022).
- [89] A. Foligno, P. Calabrese, and B. Bertini, Non-equilibrium dynamics of charged dual-unitary circuits, arXiv e-prints , arXiv:2407.21786 (2024).
- [90] R.-A. Chang, H. Shrotriya, W. W. Ho, and M. Ippoliti, Deep thermalization under charge-conserving quantum dynamics, arXiv e-prints , arXiv:2408.15325 (2024).
- [91] M. P. A. Fisher, V. Khemani, A. Nahum, and S. Vijay, Random Quantum Circuits, *Annual Review of Condensed Matter Physics* **14**, 335 (2023).